Electronic Supplementary Material (ESI) for Energy & Environmental Science.
This journal is © The Royal Society of Chemistry 2023

Supplementary Information for

Scalable manufacturing durable, tailorable and recyclable multifunctional woven thermoelectric textile system

Yuanyuan Jing[1], Jun Luo[1], Xue Han[1], Jiawei Yang[2], Qiulin Liu[2], Yuanyuan Zheng[1], Xinyi Chen[1], Fuli Huang[1], Jiawen Chen[1], Qinliang Zhuang[1], Yanan Shen[3], Haisheng Chen[3,4], Huaizhou Zhao[2,5], G. Jeffrey Snyder[6], Guodong Li[2,5]*, Ting Zhang[3,4]*, Kun Zhang[1]*

[1]Key Laboratory of Textile Science & Technology (Ministry of Education), College of Textiles, Donghua University, Shanghai, China.

[2]Beijing National Laboratory for Condensed Matter Physics, Institute of Physics, Chinese Academy of Sciences, Beijing 100190, China

[3]Institute of Engineering Thermophysics, Innovation Academy for Light-duty Gas Turbine, Chinese Academy of Sciences, Beijing, 100190, P. R. China

[4] Nanjing Institute of Future Energy System, Nanjing 211135, China.

[5]Songshan Lake Materials Laboratory, Dongguan, Guangdong 523808, China

[6]Department of Materials Science and Engineering, Northwestern University, Evanston, IL 60208, USA.

Corresponding authors: kun.zhang@dhu.edu.cn; gdli@iphy.ac.cn; zhangting@iet.cn

This file includes:

Supplementary Tables

Note S1 Configuration optimization of TET by finite element analysis (FEA)

We applied FEA simulation to optimize the TET design. Regarding the geometry of pillar (Bi_2Te_3 alloys) configuration, we fixed the pillar width of 2.5 mm for practical assembling of pillars into fabrics with stable configuration and relatively thin fabrics. We optimized the pillar height (h = 1.6, 3, and 5 mm) and inter-pillar gap (d = 3, 4, 5, and 6 mm) to maximize the cooling effect and output power density. Larger h and d values can improve the cooling effect because the thermal resistance of TE pillars and trapped air volume can be enlarged, thus leading to high cooling effect. However, it should be noted that the higher cooling effect accompanies with deteriorated COP. As h of 5 mm and d of 4 mm for TE pillars, the optimal cooling effect ~4.2 K (Fig. S1b) and COP of ~1 (Fig. S1c) for a TET unit without heat sink are achieved under quasi-steady ambient temperature of 26 °C. The output power density is optimized to be ~0.2 W/m^2 under a self-built ΔT of ~3 K (Fig. S1d). Higher thermal conductivity of fabric yarns results in slightly higher cooling effect, because it can reduce the external thermal resistance for quick heat dissipation at hot end, reducing the impact on the temperature of the cold end (Fig. S3a). The weft density in different weaving patterns including plain, twill, satin and sateen (Fig. S3b) shows negligible change in the cooling effect of TET. Increasing warp density can slightly enhance cooling effect of TET by ~1 K (Fig. S3c), owing to the increased thermal conductivity of TET. Hence, we chose the plain-woven fabric with warp density of 15.4 /cm as the textile matrix because it is easier for manufacturing and more compact for efficient heat dissipation.

Moreover, traditional heat sinks for TEDs are bulky, obtrusive, rigid and thus not even wearable, which is improper for practical applications in TET. The design of wearable heat sink has been underestimated so far. To further decrease the thermal resistance offered by air, we designed a type of wearable miniaturized heatsinks array towards enhanced cooling effect of TET (Fig. S4). More fins result in higher cooling effect, because it increases the heat dissipation area of the heat sink (Fig. S4a). The thickness of heat sink base has negligible effect on the cooling effect of TET (Fig. S4b). Increasing fin height can slightly enhance cooling effect of TET, but too large fin height is not suitable for wearables (Fig. S4c). Considering the fabrication processability and wearability, we selected the FEA-optimized geometry of 4 mm × 4 mm × 6 mm × 0.4 mm (fin thickness d_{fin}). It shows a theoretical cooling effect of ~12 K at ambient temperature of 26 °C (Fig. S4).

Note S2 Numerical analysis of thermal resistance of heat sink

The thermal resistance of heat sink can be split into two components:

$$R_{thermal\text{ - }hs} = R_{thermal\text{ - }fin} + R_{thermal\text{ - }b} + R_{thermal\text{ - }cap} \quad (2.1)$$

where $R_{thermal\text{ - }fin}$ represents the thermal resistance due to the heat conduction through the fins and convection from the fins into air[1,2]. $R_{thermal\text{ - }b}$ is the thermal resistance as the heat crosses the base plate of heat sink. $R_{thermal\text{ - }cap}$ is the capacitive thermal resistance due to air heating as it absorbs energy passing through fin channels, which can be neglected because the channel is too small. Fig. S5 shows the geometric configuration of the miniaturized heat sink.

$$R_{thermal\text{ - }fin} = \frac{1}{\eta_s h A_s} \quad (2.2)$$

where A_s specifies the heat sink surface area exposed to air, η_s is the efficiency of surface, and h is the average heat transfer coefficient. The total surface area is given by

$$A_s = nL_{hs}\left(2L_{fin} + W_{ch}\right) \quad (2.3)$$

where n is the number of channels in the microchannel heat sink, given as

$$n = \frac{W_{hs} - W_{fin}}{W_{ch} + W_{fin}} \quad (2.4)$$

The efficiency η_s is expressed as:

$$\eta_s = 1 - \frac{A_f}{A_s}\left(1 - \eta_f\right) \quad (2.5)$$

where A_f is the total fin surface area, written as

$$A_f = 2nL_{hs}L_{fin} \quad (2.6)$$

The fin efficiency η_f is defined as:

$$\eta_f = \frac{tanh\left(\sqrt{\frac{2h}{\kappa_{fin}W_{fin}}}L_{fin}\right)}{\sqrt{\frac{2h}{\kappa_{fin}W_{fin}}}L_{fin}} \quad (2.7)$$

where κ_{fin} is the thermal conductivity of the microchannel of heat sink (aluminum), which is ~237 W/m.K. In this work, $W_{fin} = 0.4$ mm, $W_{ch} = 0.5$ mm, $W_{hs} = 4$ mm, $L_{hs} = L_{ch} = 4$ mm, $L_{fin} = 5$ mm, $T_b = 1$ mm, h is set to 20 W/m^{2}K. Thus, $n = 4$, $A_s = 1.68 \times 10^{-4}$ m^2, $A_f = 1.68 \times 10^{-4}$ m^2, $\eta_f = 1$, $\eta_s = 1$, $R_{thermal-fin} = 297.6$ K/W.

$R_{thermal-b}$ is derived by conduction resistance model[3], that is

$$R_{thermal-b} = \frac{T_b}{\kappa_b A_b} \tag{2.8}$$

In this work, $A_b = 1.6 \times 10^{-3}$ m^2, $R_{thermal-b} = 2.6$ K/W, $R_{thermal-cap} = 0$, $R_{thermal-hs} = 300.2$ K/W. Because the effective heat dissipation area of this heat sink is 228 mm^2, the thermal resistance of individual heat sink is 131.8 cm^{2}K/W.

Note S3 FEA calculations of the overall thermal resistance of TET without and with heat sink

In order to study the influence of heat sink on the cooling effect of TET, we compare the overall thermal resistance of TET without and with heat sink by finite element analysis (FEA). We assume the whole system achieves a thermally steady state and heat transfer is even. For TET, the heat dissipate includes two kinds of overall heat transfer processes: one is heat transfer from the cold (bottom) to hot (top) surface of TET, one is the heat dissipate from the hot surface of TET to air.

We define the overall thermal resistance ($R_{thermal}$) of TET as[4],

$$R_{thermal\text{ - }TET} = \frac{\Delta T}{q} \qquad (3.1)$$

Where $\Delta T = T_h - T_c$, T_h is hot side temperature of TET, T_c is cold side temperature, q is the heat flux, W/m^2, $R_{thermal\text{-}TET}$ is the overall thermal resistance, cm^{2}K/W.

The average heat flux of TET without heat sink is 2158 W/m^2 (Fig. S6a) as ΔT is 15.4 K (Fig. S6b). According the equations 3.1, the effective $R_{thermal}$ of TET between hot side and cold side is 71.4 cm^{2}K/W. The surface heat flux of TET without heat sink is 158.8 cm^{2}K/W (Fig. S6c) as T_h-T_{air} is 11.4 K (Fig. S6b). According the equations 3.1, $R_{thermal\text{-}c1}$ of TET between hot side and air side is 717.4 cm^{2}K/W.

On the other hand, after the incorporation of heat sink, the average heat flux of TET with heat sink is 9093.7 W/m^2 (Fig. S6d) as ΔT is 37.4 K (Fig. S6e). According the equations 3.1, the effective $R_{thermal}$ of TET between hot side and cold side is 41.1 cm^{2}K/W. The surface heat flux of heat sink is 3088.8 W/m^2 (Fig. S6f) as T_{hs}-T_{air} is 24 K (Fig. S6e). According the equations 3.1, the thermal contact resistance between heat sink and air was calculated to be 91.6 cm^{2}K/W.

The integration of heat sink on TET adds an efficient heat dissipation channel on the TET. As finite element analysis (FEA) indicates, the overall thermal resistance of TET without heat sink is 5.9 times of that of TET with heat sink. Because of smaller overall thermal resistance of TET with heat sink, more heat can be dissipated away from TET through heat sink, resulting in better cooling effect in TET with heat sink.

Note S4 Numerical analysis of thermal resistance matching for optimized solid-state cooling and power generation

In this note, we further described the thermal resistance matching from basic thermal transfer theories to maximize the thermal resistance of TET in solid-state cooling and electrical power generation modes under specific conditions. The theoretical analysis of thermal resistance matching, which has been well developed in literature[5-7] but rarely considered in the thermal design of TET, will guide the practical configuration design of TET in this work. It should be noted that the electrical resistance matching is much simpler than that of thermal resistance matching, which has been conducted in above FEA simulations.

1. For solid-state cooling

As shown in the thermal diagram (Fig. S7a) for solid-state cooling mode, as the whole system achieves a thermally steady state, all the heat inputs and outputs are balanced at each joint in the thermal circuit[6].

At the cold side of TET close to human body surface, the heat flux (or thermal power) from body surface, Q_{body}, should be equal to the incoming heat flux at cold side of TET, Q_c.

$$Q_{body} = Q_c \tag{4.1.1}$$

$$Q_{body} = (T_{body} - T_c)/R_{thermal-c2} \tag{4.1.2}$$

$$Q_c = Q_{P,c} - 0.5I^2R_0 - (T_h - T_c)/R_{thermal-TET} \tag{4.1.3}$$

where $R_{thermal-c2}$ is the contact thermal resistance between cold side of TET and body surface, $R_{thermal-TET}$ is the total equivalent thermal resistance of TET which contributes from all components in TET as shown in Fig. S7a, the Peltier heat flux on cold side of TET is defined as $Q_{P,c} = S_{TET} * I * T_c$.

From equations (4.1.1)-(4.1.3), we can deduce the following formula of as a function of T_c and ΔT in a given application conditions.

$$1/R_{thermal-TET} = \left(S_{TET} * I * T_c - 0.5I^2R_0\right)/(T_h - T_c) - (T_{body} - T_c)/R_{thermal-c2}/(T_h - T_c) \tag{4.1.4}$$

We calculated the thermal resistance of TET unit (1 cm^2) with respect to T_c and ΔT under the following conditions. For instance, the intrinsic parameters S_{TET} = 0.84 mV/K, R_0=0.088 ohms for TET unit (1 cm^2) with two pairs of *p*-type and *n*-type TE pillars, and external parameters: input DC value I = 0.6 A (for TET without heat sinks) or 1.6 A (for TET with heat sinks), T_{body}=34 ^{o}C, and the thermal conductance at human body surface is 20 W/m^{2}K.

The calculation results are shown in Fig. S7b-S7c. It can be seen that the thermal resistance of TET should be at least ~106.5 cm^2K/W (Fig. S7b) for effective dissipating heat from hot side of TET to air as the simulated temperature difference ΔT is 14 K, which corresponds to the measured temperature values in our TET sample without heat sinks (T_h=314.45 K, T_c=304.25 K, $T_h - T_c$ =14.3 K, I=0.6 A). If there are heat sinks for each pillar, the thermal resistance of TET should be at least ~91.4 cm^2K/W (Fig. S7c) for effective dissipating heat from hot side of TET to heat sinks as the simulated temperature difference ΔT is 25 K, which corresponds to the measured temperature values in our TET sample with heat sinks (T_h=323.55 K, T_c=298.65 K, $T_h - T_c$ =24.9 K, I=1.6 A).

Similarly, at hot side near air

$$Q_{air} = Q_h \tag{4.1.5}$$

$$Q_{air} = (T_h - T_{air})/R_{thermal-c1} \tag{4.1.6}$$

$$Q_h = Q_{P,h} + 0.5I^2R_0 - (T_h - T_c)R_{thermal-TET} \tag{4.1.7}$$

where $R_{thermal-c1}$ is the contact thermal resistance between hot side of TET and air, T_h is larger than T_{air}, and the Peltier heat flux is defined as $Q_{P,h}=S_{TET}*I*T_h$.

From equations (4.1.5)-(4.1.7), we can deduce the following formula of as a function of T_h and ΔT in the given thermoelectric properties of TET, T_{air}=37 °C. $R_{thermal-c1}$ of TET between hot side and air is set to be 717.4 cm^2K/W for TET without heat sinks while $R_{thermal-c1}$ of TET between hot side and heat sink is set to be 113.8 cm^2K/W for TET with heat sinks, as calculated in Note S2.

$$1/R_{thermal-TET} = (S_{TET} * I * T_h + 0.5I^2R_0)/(T_h - T_c) - (T_h - T_{air})/R_{thermal-c1}/(T_h - T_c) \tag{4.1.8}$$

It is noted that Q_{air} is directing to the air, meaning the heat transfer from hot side of TET to air because T_h is larger than T_{air}. In order to keep this happens, the outgoing heat flux Q_h should be larger than Q_{air}. This is because that if the thermal resistance of TET is smaller than its critical value, then the heat will flow back into TET.

We thus calculated the thermal resistance of TET unit (1 cm^2) with respect to T_h and $T_h - T_c$ under the above conditions. The calculation results are shown in Fig. S7. It can be seen that the thermal resistance of TET without heat sinks should be at least ~83.0 cm^2K/W (Fig. S7d) for effective dissipating heat from hot side of TET to air as the simulated temperature difference ΔT is 14.3 K, which corresponds to the measured values in our TET sample (T_h=314.45 K, T_c=304.25 K, $T_h - T_c$ =14.3 K, I=0.6 A). If there are heat sinks for each pillar, the thermal resistance of TET should be at least ~58.8 cm^2K/W (Fig. S7e) for effective dissipating heat from hot side of TET to air as the simulated temperature difference ΔT is 25 K, which corresponds to the measured values in our TET sample (T_h=323.55 K, T_c=298.65 K,

T_h - T_c =24.9 K, I=1.6 A). These numerical results agree well with the FEA-simulated thermal resistances of TET is 71.4 cm^{2}K/W and 41.1 cm^{2}K/W for TET without or with heat sinks, respectively.

Meanwhile, the typical metabolic rate Q_{body} of human body ranges from ~70 W/m^2 for sedentary activities to ~440 W/m^2 for strenuous exercises[7,8]. The thermal resistance of human body is typically larger than 100 cm^{2}K/W but varies for different locations and ambient conditions. For instance, body chest can possess a thermal resistance of 130-200 cm^{2}K/W. The air can offer a thermal resistance of ~500 cm^{2}K/W at h_{air} of 20 W/m^{2}K to thermoelectric devices.

Hence, based on the calculation and discussion, we can expect that the effective thermal resistance of TET should be at least 106.5 cm^{2}K/W for active solid-state cooling under the afore mentioned operation conditions. Furthermore, we also can conlude that the addition of heat sinks on hot side of TET can dramatically enhance the heat dissipation capability under solid-state cooling mode, and the required thermal resistance of TET is smaller than that of TET without heat sinks.

2. For thermoelectric power generation

As seen Fig. S8a, the thermal diagram for power generation mode is slightly different to that of solid-state cooling mode. The TET typically works at cold weather for thermoelectric power generation, meaning the hot side of TET is near human body skin while the cold side is exposed to air.

The electrical and thermal matching conditions have been developed in previous reports[5]. Assuming the electrical resistance matching has been satisfied with the optimal resistance ratio

$$R/R_0 = \sqrt{1 + Z\overline{T}}\ ;\quad Z\overline{T} = S_{TET}^2/R_0K_{TET} \qquad (4.2.1)$$

where R is the load resistance. We can write the generated power output of TET as

$$P = I^2R \qquad (4.2.2)$$

$$I = S_{\mathrm{TET}} * (T_h - T_c)/(R_0 + R) \qquad (4.2.3)$$

$$T_h - T_c = (T_{core} - T_{air})K_{ext}/(K_{TET} + K_{ext}) \qquad (4.2.4)$$

where $Z\overline{T}$ is the so-called average device ZT, where $\overline{T}$ is the average temperature of T_{core} and T_{air}, which is defined as (T_{core}+T_{air})/2, I is the generated direct current, and K_{TET}, K_{ext} are the thermal conductance of TET unit and the sum of external thermal conductance contributed from human body, air and interfaces between them. Note: This current is different from the one in calculation for solid-state cooling mode.

From equations (4.2.1)-(4.2.4), we can re-write the power output of TET as

$$P = \frac{S_{TET}^2(T_{core} - T_{air})^2\sqrt{1 + Z\overline{T}}}{R_0(1 + \sqrt{1 + Z\overline{T}})^2(K_{TET}/K_{ext} + 1)^2} \qquad (4.2.5)$$

Based on equation (4.2.5), we can numerically calculate the power output and temperature difference T_h-T_c on TET as a function of T_{air} and K_{TET} (or $R_{thermal\ -\ TET}$). The calculated results are shown in Fig. S8b-8c. We can find that the simulated power output increases as T_{air} and $R_{thermal\ -\ TET}$ increase. For TET without heat sinks, where the cold side of TET exposing to the air, the TET can generate a power density of ~0.33 W/m^2 (Fig. S8b) as T_{air} is 26 ^{o}C, which is similar to the power output in Fig. S1d and Fig. 8b, the corresponding thermal resistance of TET is 117.6 cm^{2}K/W. For TET with heat sinks, where the cold side of heat sink on TET exposing to the air, the TET can generate a power density of ~3.36 W/m^2 (Fig. S8c) as T_{air} is -3 ^{o}C and the corresponding thermal resistance of TET is 63.9 cm^{2}K/W.

Based on all above FEA and numerical analysis, we can expect that TET without heat sink possessing large enough thermal resistance, which is larger than 117.6 cm^{2}K/W in this case, or efficient heat dissipation via heat sink, can produce high thermoelectric cooling and power generation performances.

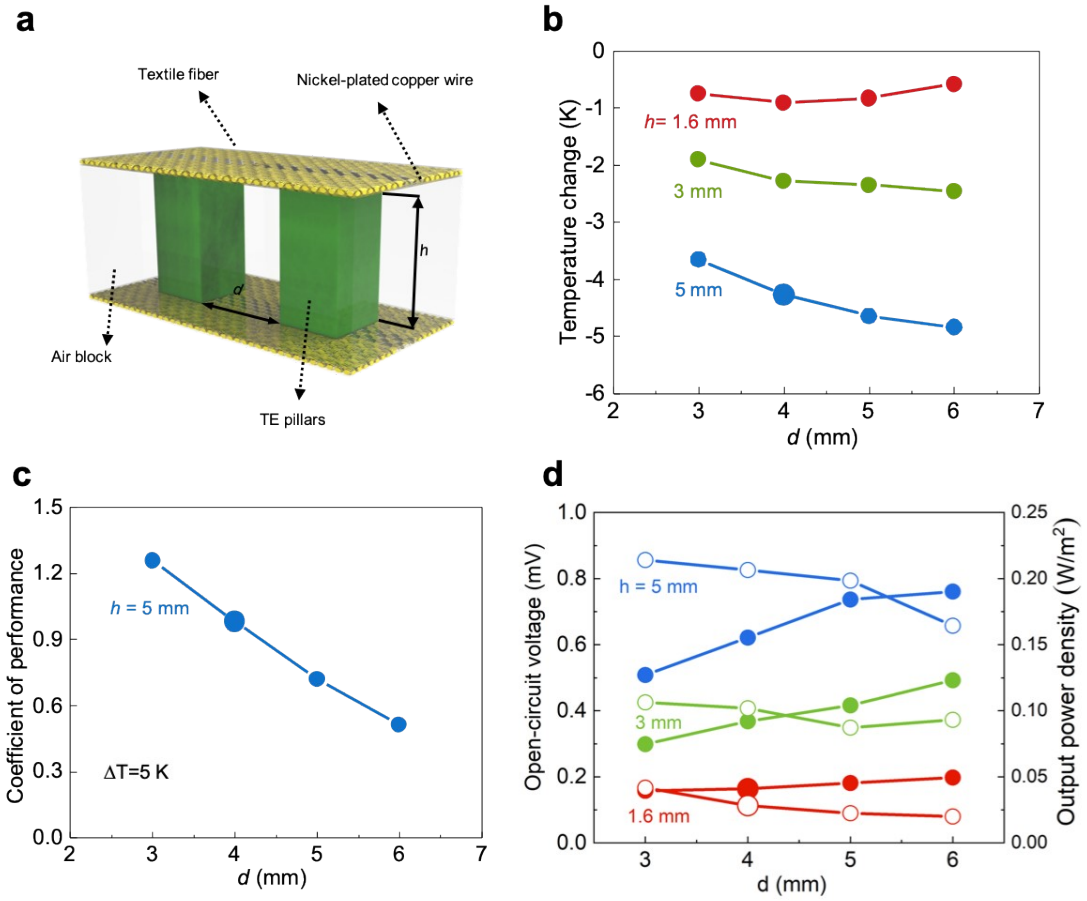

Fig. S1. Theoretical optimization of geometrical dimensions of TE pillars for cooling effect and thermoelectric power generation. (**a**) The model of TET unit for finite element analysis. The unit cell of TET contains top and bottom plain woven fabrics, *p*-type and n-type TE pillars and solder-coated copper wires (0.1 mm in diameter) and an air gap. (**b**) Maximum simulated cooling effects with respect to various TE pillar height (*h*) and pillar space (*d*) values. The cooling effect is enhanced with increased *h* up to 5 mm while there is an optimum *d* to maximize the cooling effect. (**c**) Corresponding maximum simulated COP values with respect to various TE gap (*d*) values at ΔT~5 K and DC of 0.6 A. (**d**) Coherent maximum output voltage (circle dots) and power density (solid dots) with respect to various TE pillar height (*h*) and TE gap (*d*) values at ΔT = 5 K. Note: All these simulations are based on TET unit without heat sinks under natural convection. For cooling: The environment temperature is 26 °C, the convection coefficient of internal TET is 1.8 W/m^2·K, the convection coefficient close to TET hot surface is 20 W/m^2·K. For power generation: The temperature difference is self-built as the heat source temperature is set to be 35 °C, and the environment temperature is 26 °C. The convection coefficient close to TET cold surface is set to be 20 W/m^2·K.

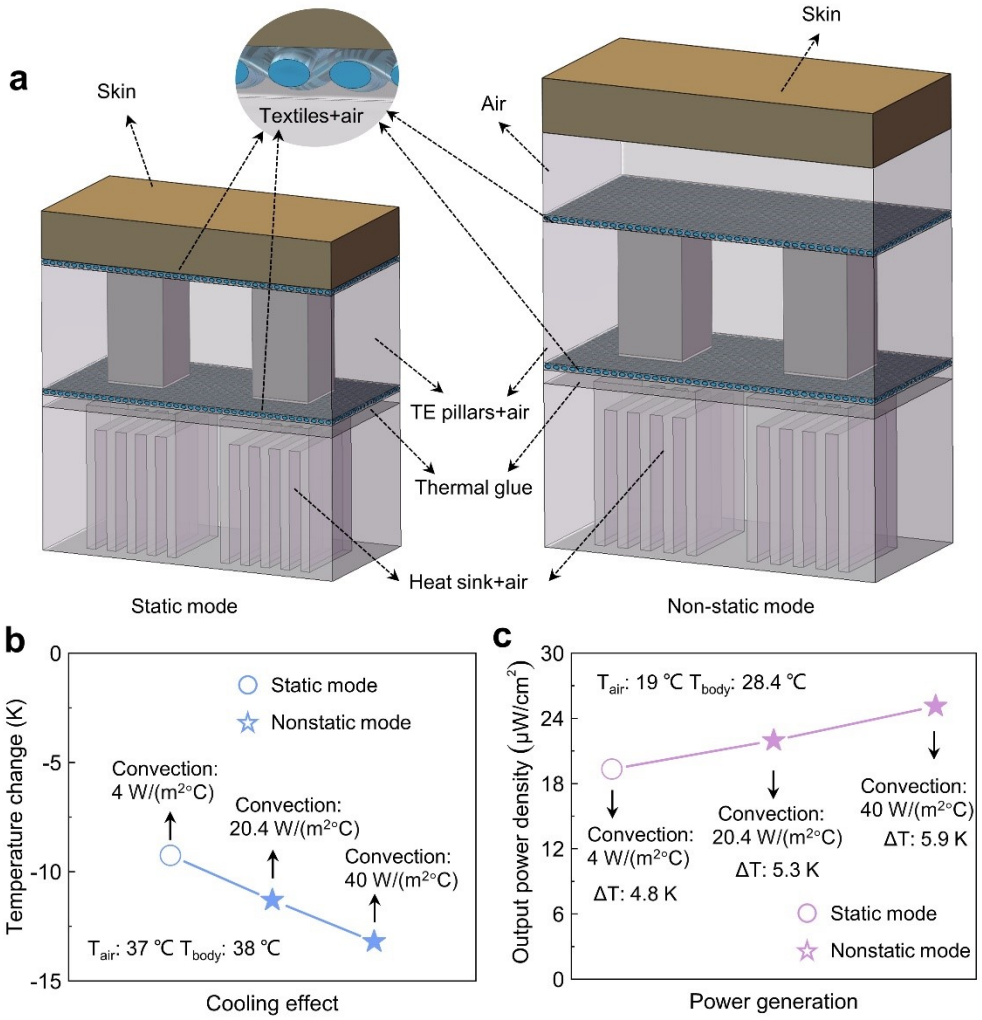

Fig. S2. Theoretical simulation of cooling effect and thermoelectric power generation of TET in non-static mode. (**a**) TET models in static and non-static modes. The simulated cooling effect (**b**) and power generation (**c**) of TET model in non-static mode. Note: ΔT is the actual temperature difference on TET.

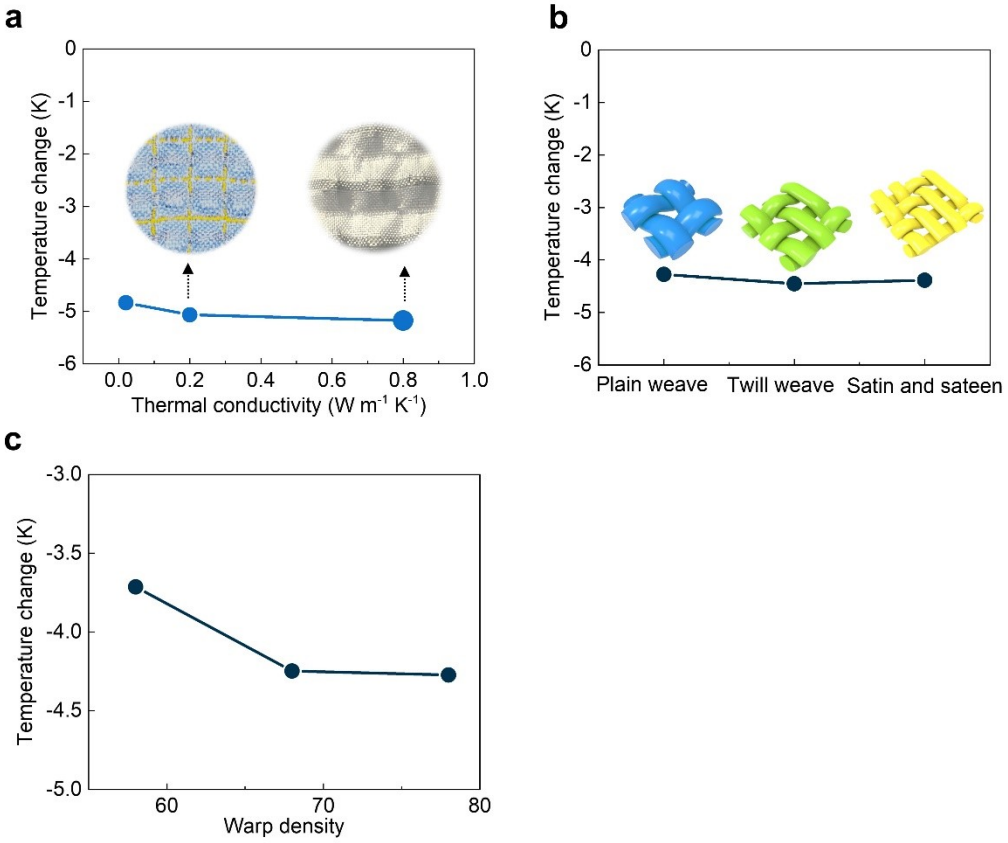

Fig. S3. Theoretical optimization of fabric structures for cooling effect of TET unit. (**a**) The cooling effects of TET with respect to different thermal-conductivity yarns under the same textile structure and warp density. (**b**) Maximum cooling effects with respect to various textile structures: plain weave (blue), twill weave (green), satin and sateen weave (yellow) under the same thermal-conductivity yarns (0.337 W/m·K) and warp density. (**c**) Maximum cooling effects with respect to various warp densities under the same textile structure and thermal-conductivity yarns (0.337 W/m·K). Note: All these simulations are based on TET unit without heat sinks under natural convection. For cooling: The environment temperature is 26 ^{o}C, and the convection coefficient of TET surface is 20 W/m^{2}·K.

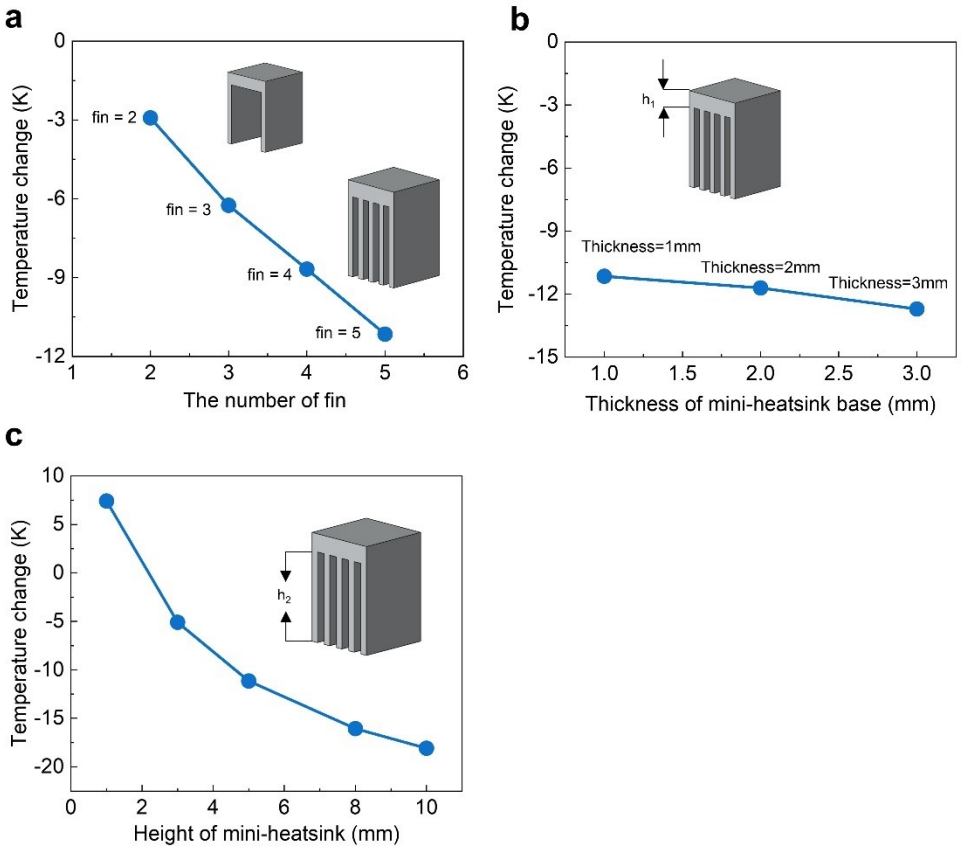

Fig. S4. Theoretical optimization of the geometrical dimensions of miniaturized heat sink for enhanced cooling effect of TET. (a) At a constant value of heatsink fin width (0.4 mm), the cooling effect of TET is altered with respect to different fin numbers. (**b**) The cooling effect of TET unit with respect to heat sinks with different base thicknesses. (**c**) The cooling effect of TET unit with respect to different fin heights of heat sink. Note: The heat sink is made of 6063 Al alloy. The environment temperature is 26 ^{o}C, and the convection coefficient of surface of TET is 20 W/ m^{2}·K.

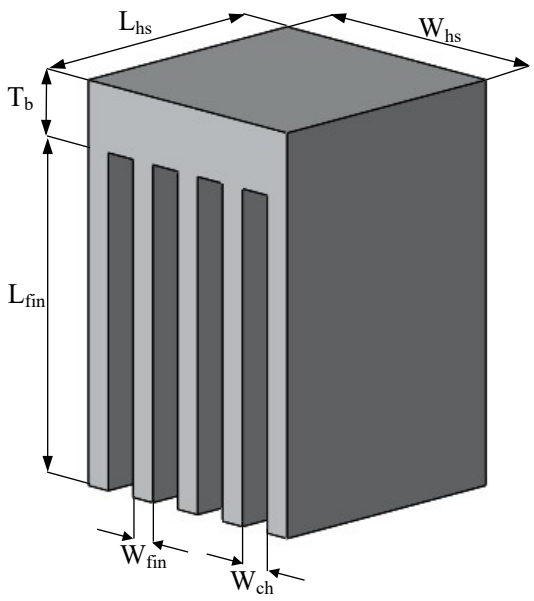

Fig. S5. Schematic of microchannel heat sink

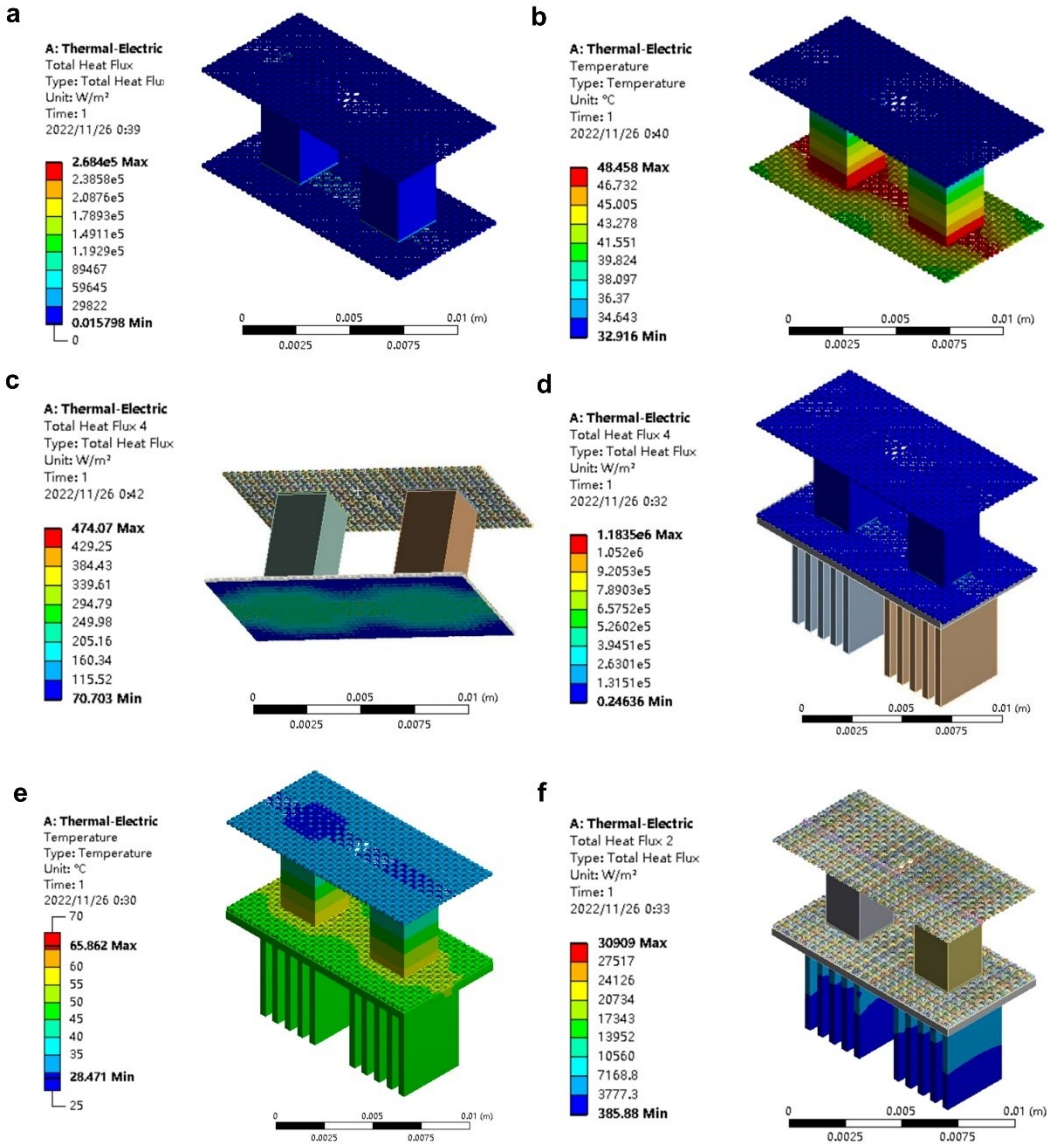

Fig. S6. The heat flux and temperature range of TET without and with heat sink. (a) The heat flux in TET without heat sink. **(b)** The temperature range of TET without heat sink. **(c)** The surface heat flux between hot surface to air of TET without heat sink. **(d)** The heat flux in TET with heat sink. **(e)** The temperature range of TET with heat sink. **(f)** The surface heat flux between heat sink to air of TET with heat sink. The environment temperature is 37 ^{o}C, the heat flow close to human body surface is 20 W/m^2, the body surface temperature is 34 ^{o}C, the convection coefficient of air close to hot surface of TET is 20 W/m^2·K, the convection coefficient of air close to heat sink surface is 20 W/m^2·K. The input direct current for TET without heat sink is 0.6 A. The input direct current for TET with heat sink is 1.6 A.

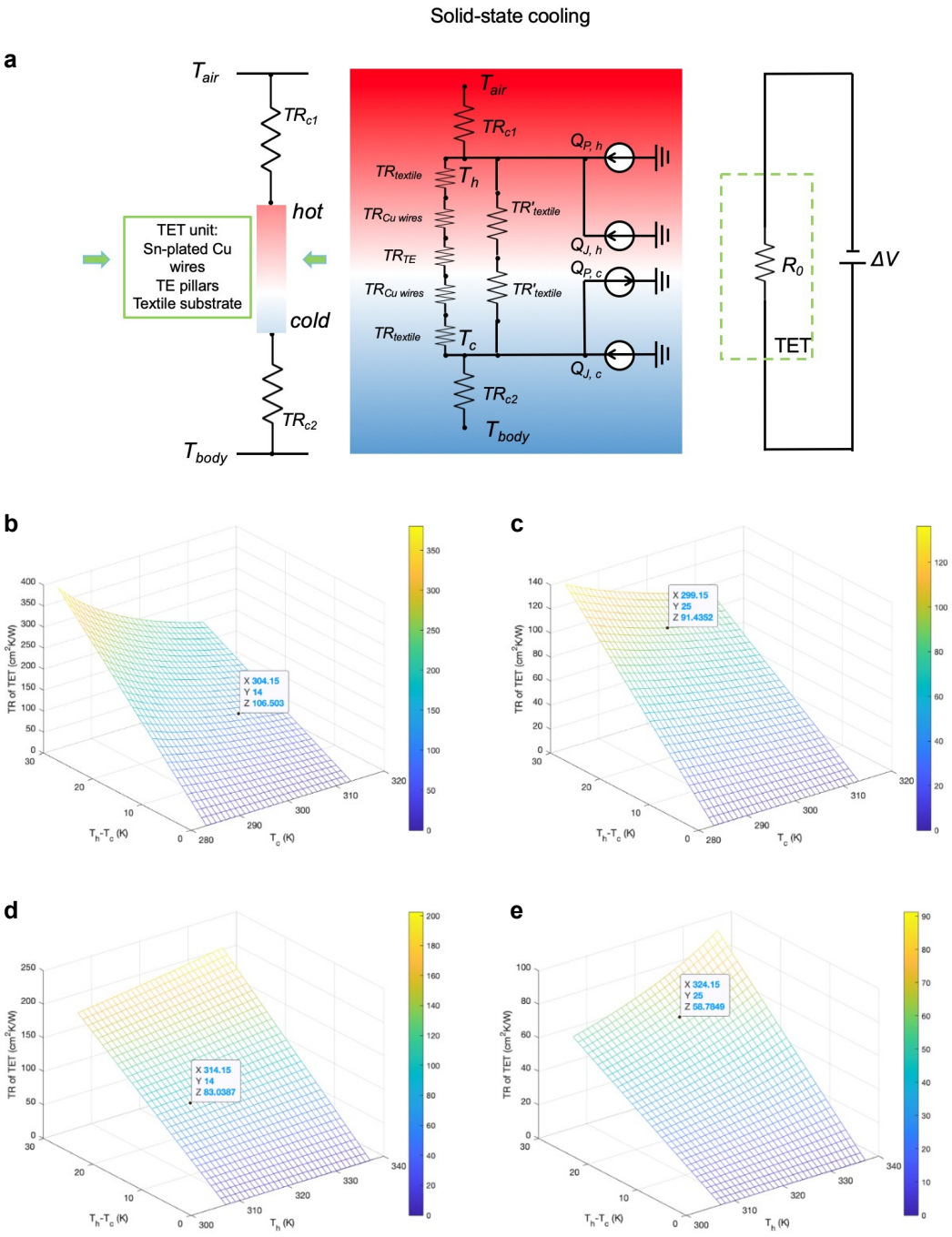

Fig. S7. The simulated thermal resistance of TET for solid-state cooling (a) The thermal and electrical circuit of TET for solid-state cooling mode. The simulated thermal resistance of TET **(b)** without heat sink, **(c)** with heat sink as a function of T_c and T_h-T_c under specific conditions in this work. The simulated thermal resistance of TET **(d)** without heat sink, **(e)** with heat sink as a function of T_h and T_h-T_c under specific conditions in this work.

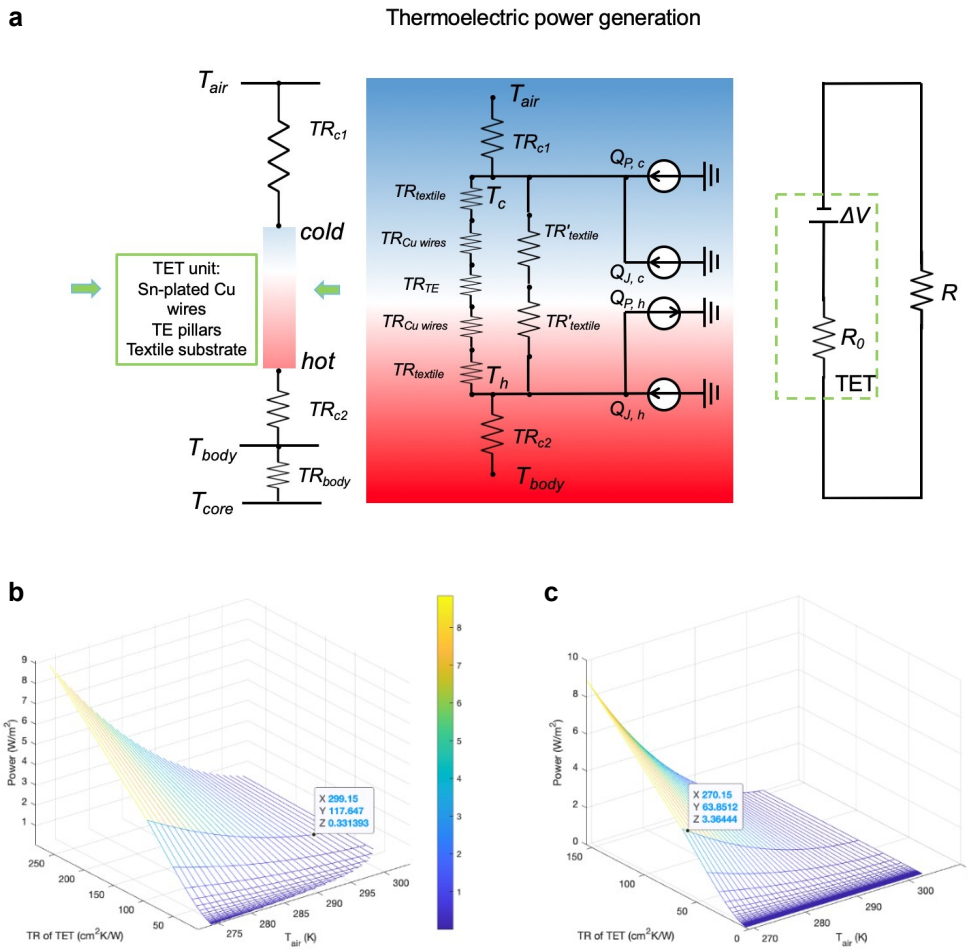

Fig. S8. The simulated power output of TET for thermoelectric power generation. **(a)** The thermal and electrical circuit of TET for thermoelectric power generation mode, The simulated power output of TET **(b)** without heat sink, **(c)** with heat sink as a function of T_{air} and $R_{thermal-TET}$ under specific conditions in this work.

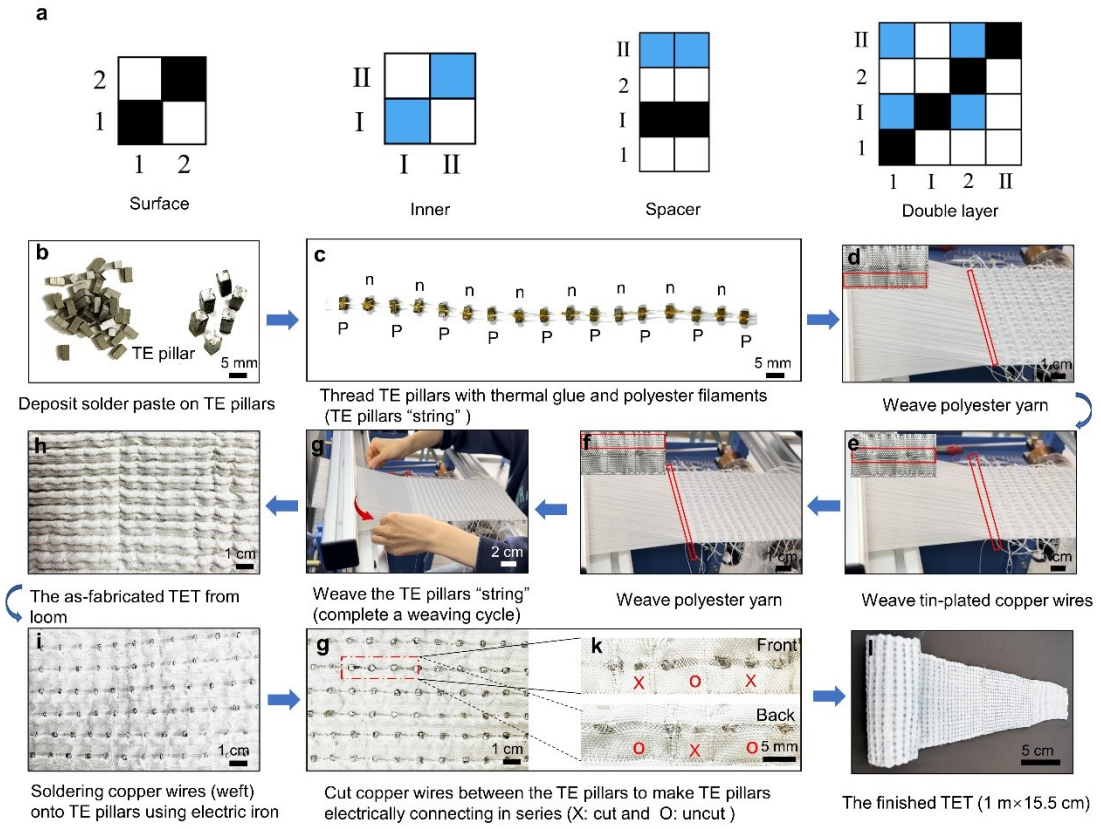

Fig. S9. The structure design and textile manufacturing of TET. (a) Organization chart of bilayer woven fabric: surface layer (black) and inner layer (blue). **(b-i)** The manufacture process of TET (15.5 cm × 1 m) using a semi-automatic weaving loom. Note: The structure parameters of TE pillars and textile fabric involved in the textile manufacturing process are based on the optimized geometry and dimensions in theoretical simulations.

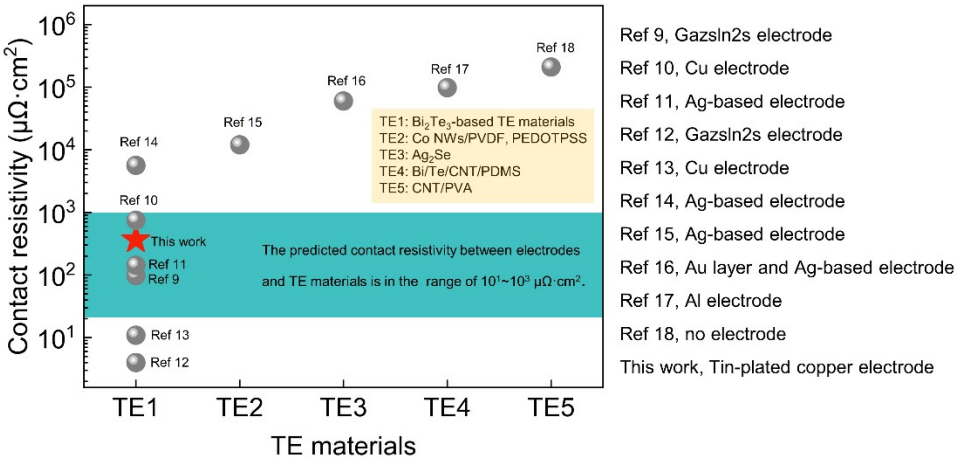

Fig. S10. The comparison of contact electrical resistivity in this work with reported in literatures.

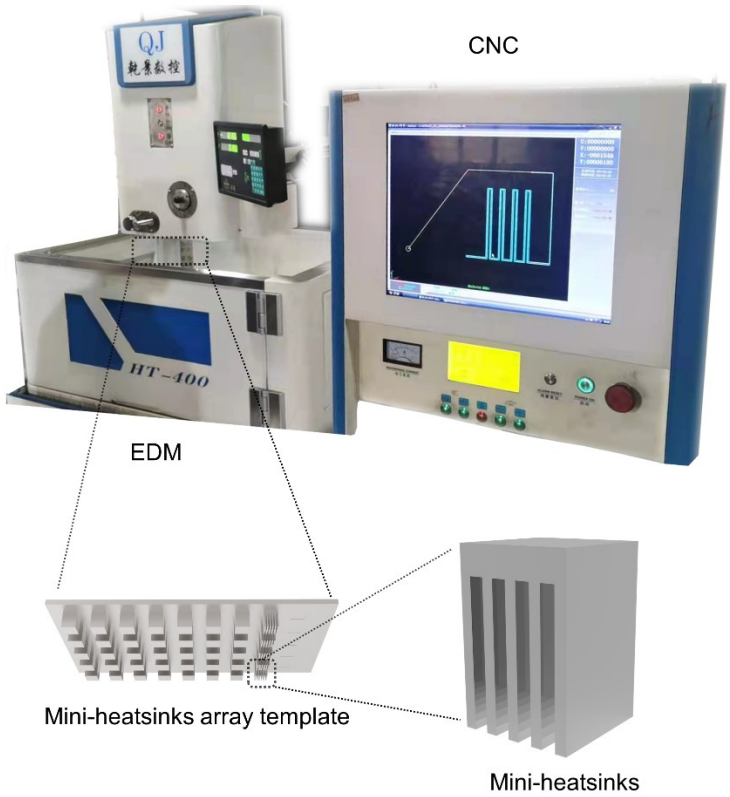

Fig. S11. Schematic diagram of the machining process of mini-heatsinks. The miniaturized heatsinks based on 6063 Al alloy were machined with computerized numerical control (CNC) and wire electric discharge machining (EDM) processes.

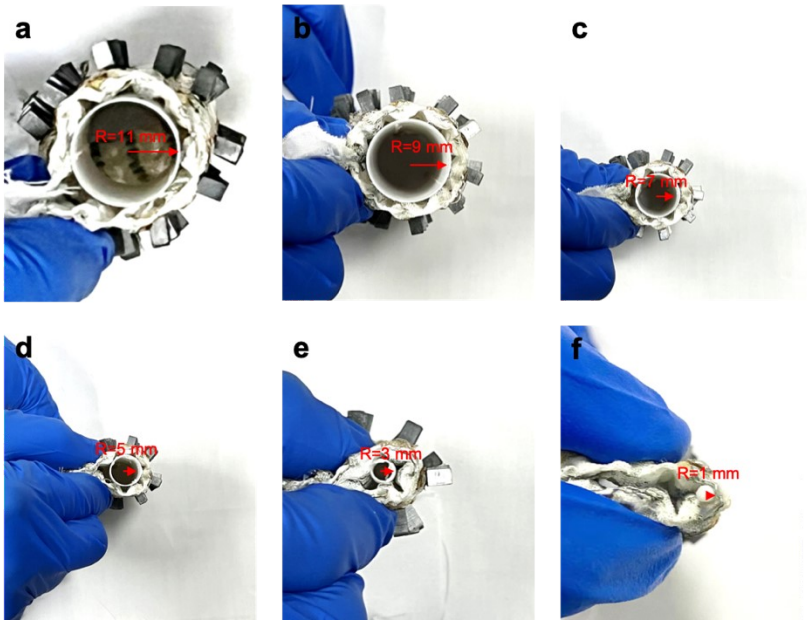

Fig. S12. Optical images of different bending radii of TET system. The minimum bending radius of the TET can reach to 1 mm, which can fully meet the wearing requirements of the human body.

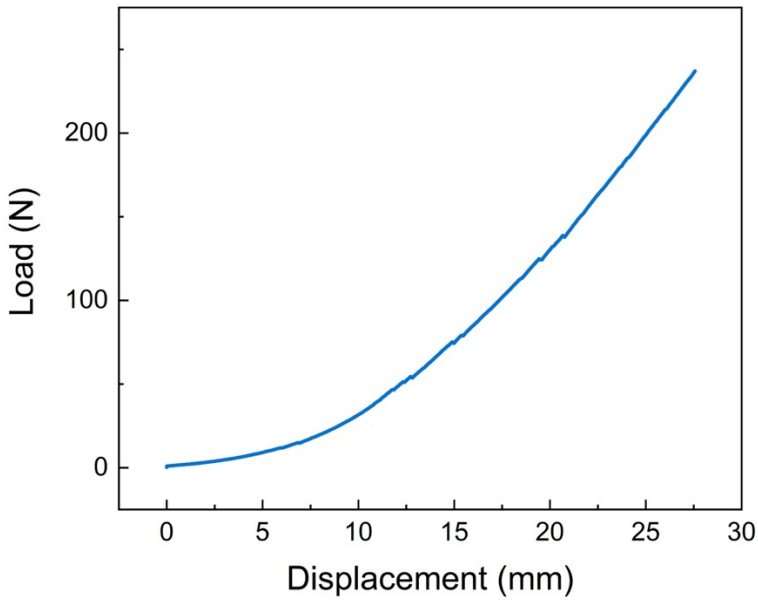

Fig. S13. The load change of TET sample with respect to the displacement during tensile stressing.

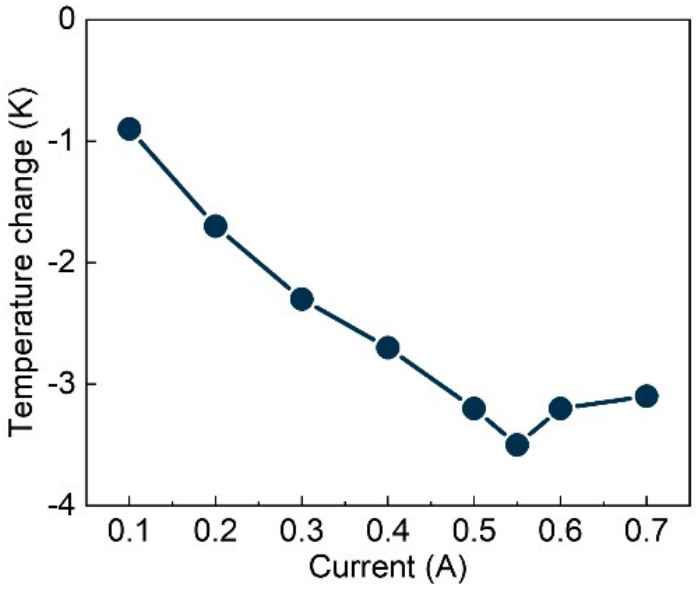

Fig. S14. The cooling effect of TET without heat sinks after the 20th washing cycle.

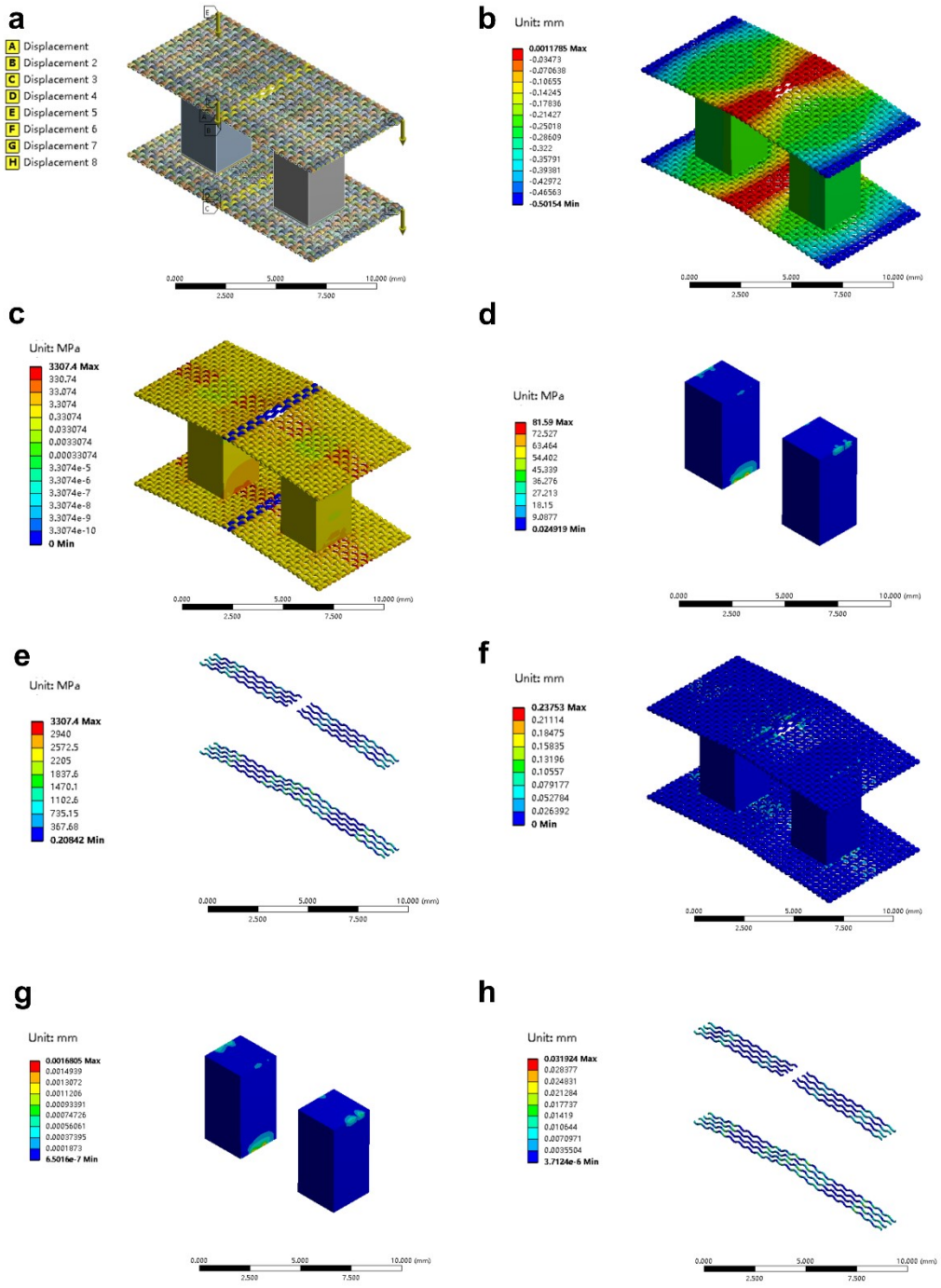

Fig. S15. The FEA simulation of mechanical stability of TET under three-point bending. (a) The model and operation principle of TET unit. (**b)** The total deformation of TET unit upon three-point bending. (**c)** The stress distribution of the whole TET unit, **(d)** TE pillars and **(e)** nickel-plated copper wires in TET unit. **(f)** The strain distribution of the whole TET unit, **(g)** TE pillars and **(h)** nickel-plated copper wires in TET unit.

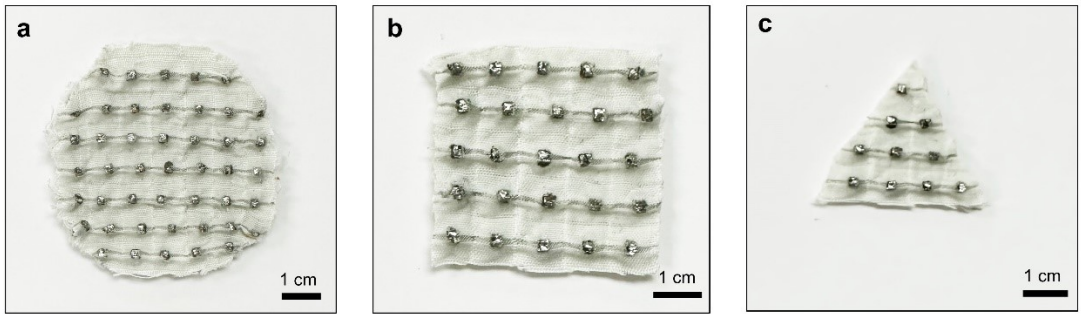

Fig. S16. Demonstration of tailor ability of TET with arbitrary shapes: circle (**a**), square (**b**) and triangle (**c**).

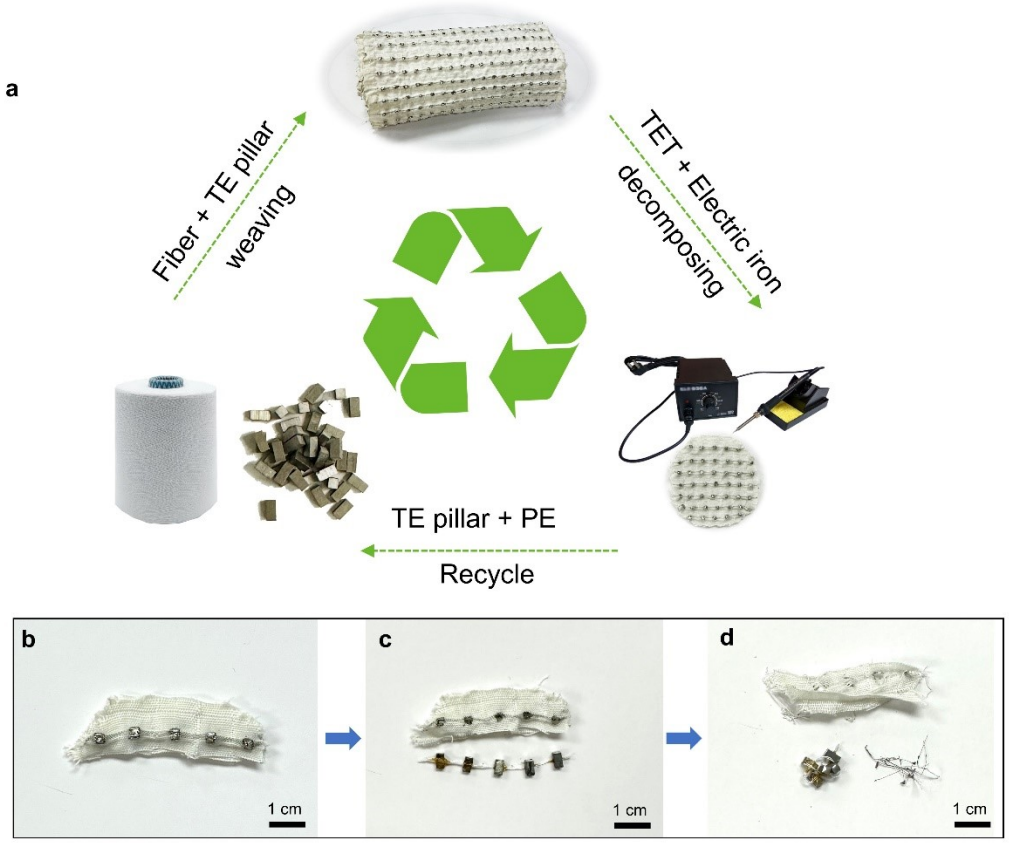

Fig. S17. Recycle process of Bi_2Te_3 based TET. (**a**) A diagram of recycle process of TET, (**b-d**) Physical disassembling process of TET：(**b**) A small unit of TET, (**c**) Heating the weld and disassemble the TE pillars, (**d**) Removing the tin-plated copper wires from fabric.

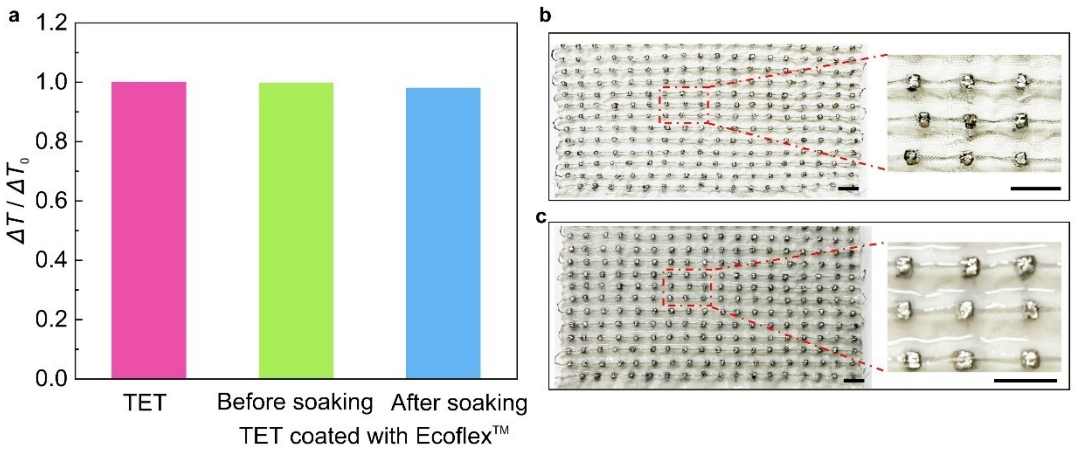

Fig. S18. (**a**) Comparison of cooling effects of TETs. Note: TET coated with Ecoflex™ soaked in sodium chloride solution (0.9 wt%) for 16 hours and left to dry at room temperature. (**b-c**) Optical images of TET without Ecoflex™ coating (**b**) and TET with Ecoflex™ coating (**c**). Scale bar: 10 mm

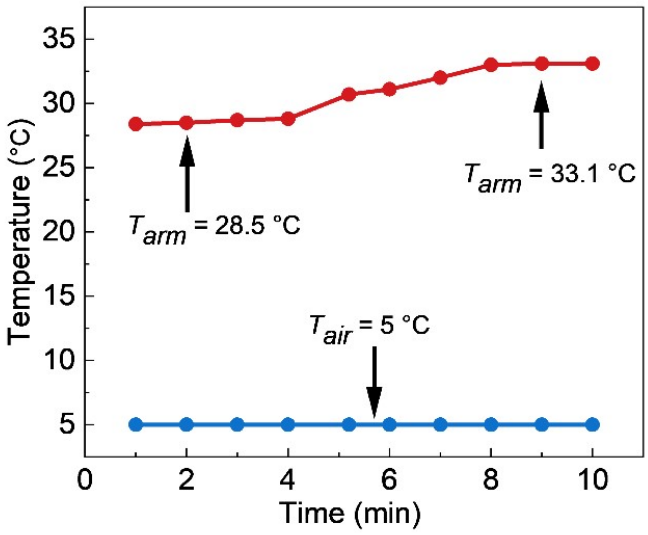

Fig. S19. The heating effect of TET system in cold environment. TET system can continuously warm up the human body in a low-temperature environment (5 °C).

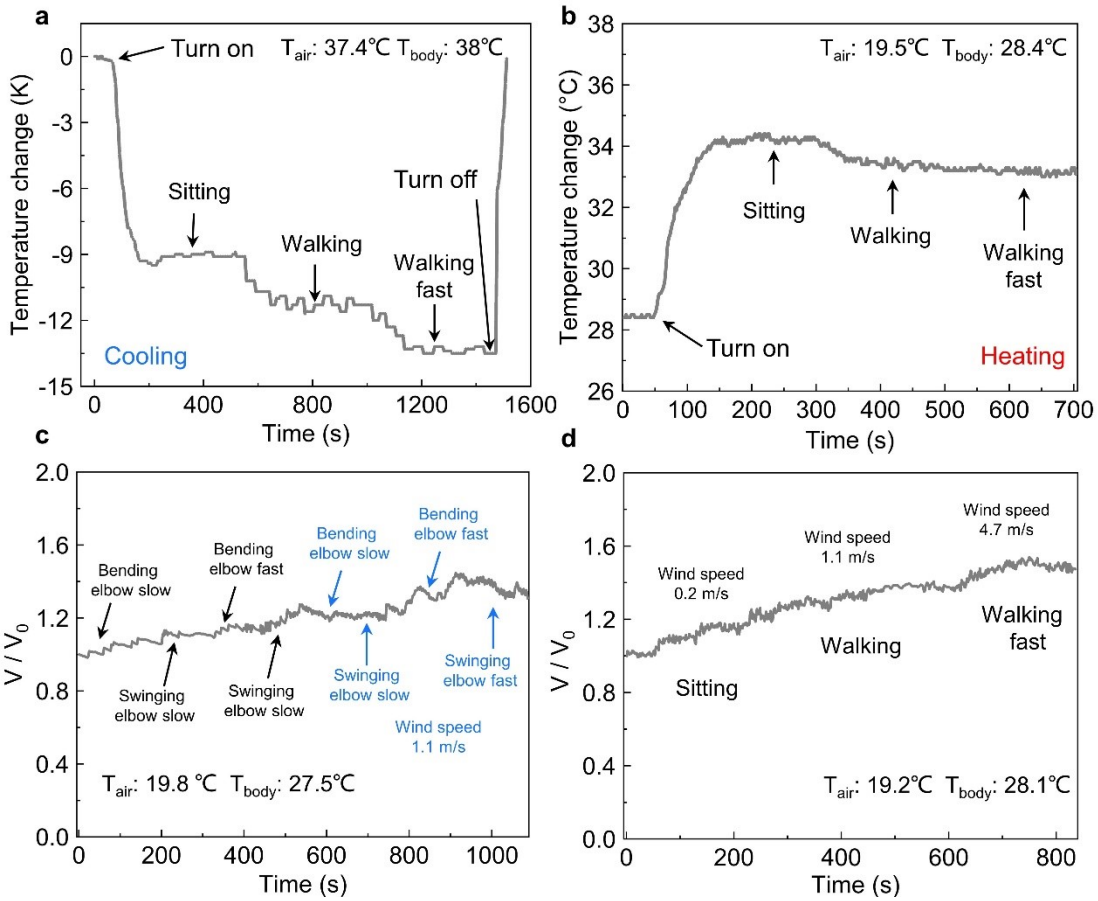

Fig. S20. The thermoelectric performance of TET system under body motions. The cooling effect (**a**) and heating (**b**) of TET on body chest. The output voltage changes of TET worn on elbow (**c**) and chest (**d**).

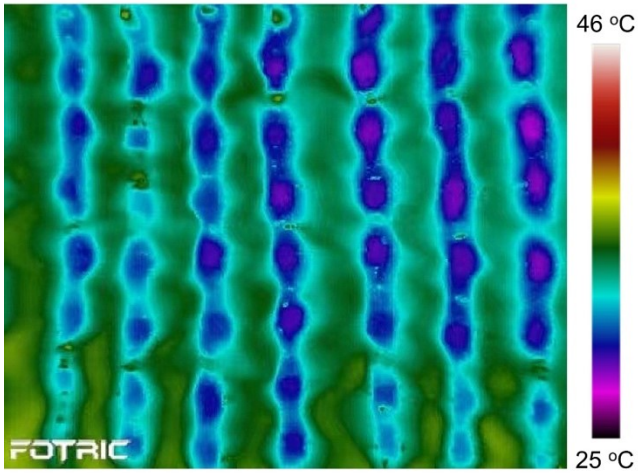

Fig. S21. IR image of TET without heat sink. It displays the inner surface temperature mapping at the optimized DC current of 0.55 A.

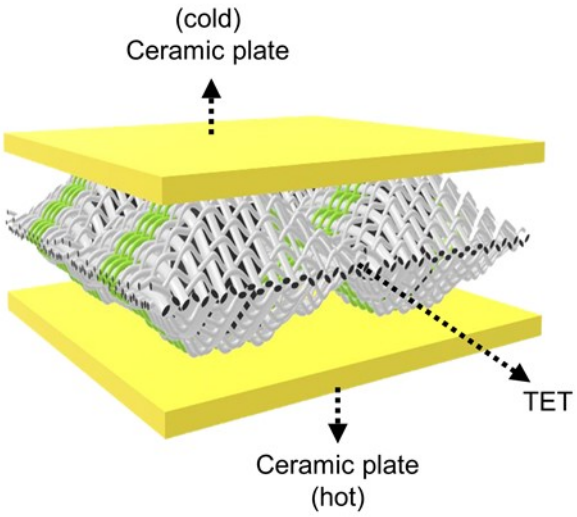

Fig. S22. Diagram of the COP measurement of TET by using Mini-PEM (ADVANCE RIKO, Japan) system. Note: The good thermal contact between TET and ceramic plates were achieved by using thermal paste.

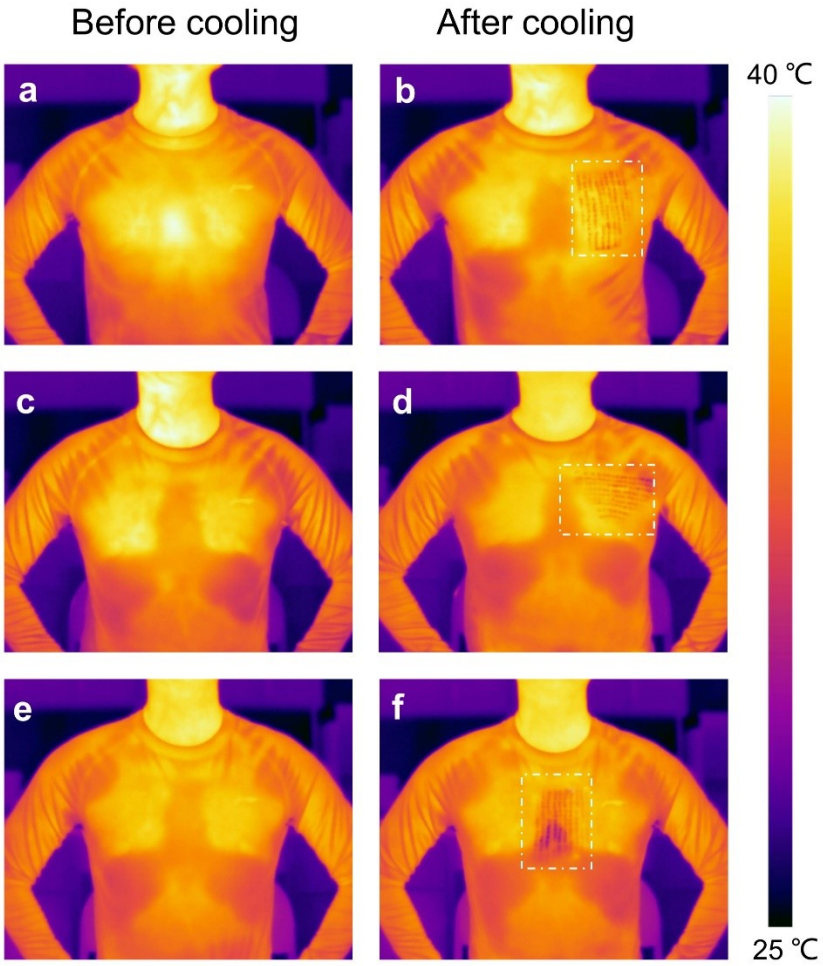

Fig. S23. IR image of body surface temperature before covering TET and after removing the TET system. (**a-d**) TET was placed on the left chest in different alignments (**a-b**, vertical alignment; **c-d**, horizontal alignment). (**e-f**) TET was placed on the middle chest.

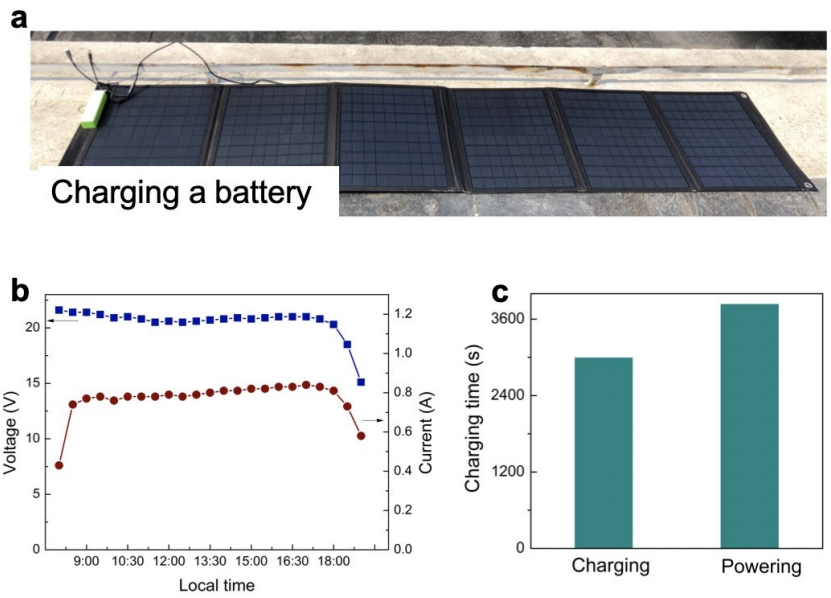

Fig. S24. The wearable solar panel powering a portable battery for TET. (a) The unfolded solar panel charging a portable battery (2600 mAh) under solar irradiation. Note: The UV index was 7 on 15:00, 11th June, 2021, Shanghai, Sunny. The size of the amorphous silicon based solar panel is 16.5 cm✕29cm (folded) and 123 cm✕29cm (unfolded). It should be mentioned that small-size single-crystal silicon based solar panel with comparable power density can be used for higher portability. **(b)** The generated solar voltage and current with respect to the local time. **(c)** shows the powering time of portable battery as charged by solar panel for TET is longer than the charging time of portable battery by solar panel.

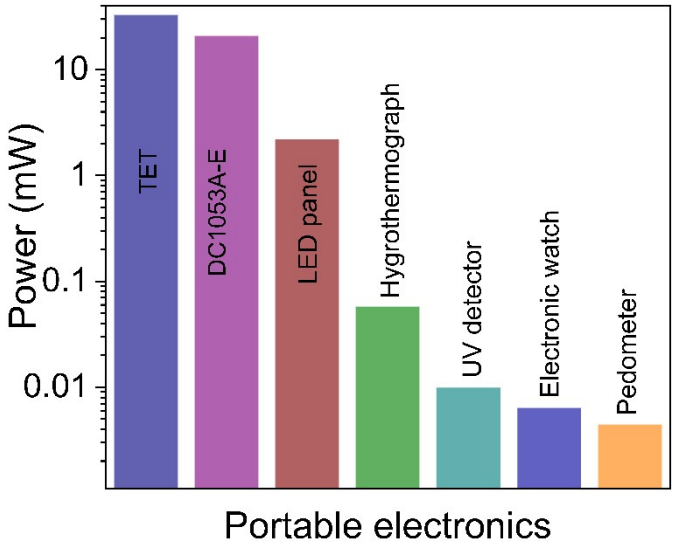

Fig. S25. The summary of output power of TET on human skin and power consumption for some portable low-power electronics.

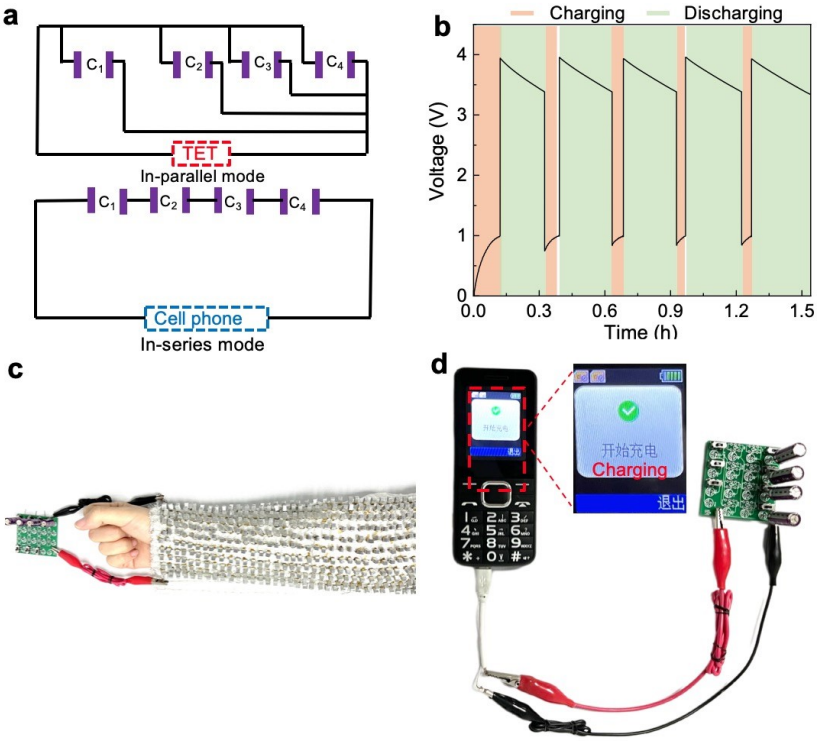

Fig. S26. Demonstration of charging a cell phone with supercapacitor array. a, The charging and powering modes of supercapacitor array. **b,** The charging and discharging curve of the supercapacitor array powered by TET (ΔT~14.4 K). **c-d**, Demonstration of TET powering a cell phone on human skin.

Supplementary Tables

Table S1 Details of corresponding materials' parameters used in FEA of TET unit for solid-state cooling and thermoelectric power generation

Materials	κ (W/m·K)	ρ (Ω·m)	S (μV/K)
p-type pillar	1.3	1×10^{-5}	210
n-type pillar	1.65	1×10^{-5}	-210
Yarn	0.337	/	/
Tin-plated copper wire	400	1×10^{-8}	/
Solder	67	1.14×10^{-7}	/
Al	237	2.85×10^{-8}	/
Air	0.025	/	/
Thermal paste	1.2	/	/

Table S2 The calculation of internal electrical resistance of TET with 100 pairs of TE pillars

	σ (S/cm)	A (cm^2)	L (cm)	N	R (Ω)
p-type pillar	1000	0.0625	0.5	100	0.8
n-type pillar	1000	0.0625	0.5	100	0.8
Tin-plated copper wire	1.1×10^{6}	$4\times7.85\times10^{-5}$	0.9	200	0.52
Solder	1.14×10^{5}	0.0625	0.1	400	5.6×10^{-3}
Contact resistance	/	/	/	400	2.27
Total resistance					4.4

Note:

(1) σ, A, L, N and R are the electrical conductivity, cross-section area, length, number and electrical resistance of each component.

(2) Total contact resistance = (Total R of TET) - (R of all *p*-type pillars) - (R of all *n*-type pillars) - (R of all nickel-plated copper wires) - (R of solder).

(3) Single contact resistance for each pillar = (Total contact resistance)/N=2.27/400=5.7 mΩ.

(4) Contact resistivity=5.7 mΩ × 0.0625 cm^2=356 μΩ·cm^2

Table S3 Details of corresponding materials' parameters used in the mechanical stability of TET unit by FEA

Materials	Young's modulus (GPa)	Poisson's ratio	Yield strength (MPa)	Density (g/cm^3)
p-type pillar	50	0.22	/	6.64
n-type pillar	50	0.22	/	7.69
Textile yarn	0.45	0.4	/	0.03 g/m
Tin-plated copper wires	106	0.33	39200	8.963
Solder	44.5	0.3	48	7.28

Table S4 The calculation of total thermal conductance (κ') of TET (15 cm × 9 cm)

Component No.	Components in TET	*Surface area A* (m^2)	*Thickness L* (m)	*Thermal conductivity* κ (W/m.K)	*Numbers N*	*Thermal conductance* κ' (W/K)
p	*p*-type pillar	6.25×10^{-6}	0.005	1.3	100	1.63×10^{-3}
n	*n*-type pillar	6.25×10^{-6}	0.005	1.65	100	2.06×10^{-3}
1	Tin-plated copper wire	3.16×10^{-8}	0.0001	400	200	0.126
2	Solder on one pillar	6.25×10^{-6}	0.0005	67	400	0.838
3	Top/bottom textile substrate on one pillar	6.25×10^{-6}	0.00014	0.078	400	3.48×10^{-3}
4	Top/bottom textile substrate between pillar gap with trapped air	9.90×10^{-5}	0.00014	0.078	200	5.52×10^{-2}
5	Air among top and bottom textile substrate between pillar gap	9.90×10^{-5}	0.00472	0.025	100	5.24×10^{-4}
6	Bonded textile substrate not on TE segment without air	1.10×10^{-5}	0.00028	0.078	100	3.06×10^{-3}
	κ'_{total}					**0.5335**
	Thermal resistance (cm^2K/W)					**253.0**

Note:

(1) All the areas for each component in the above table is based on single p-type or n-type TE segment.

(2) *N*, *A*, *L* and κ are the number, area, length and thermal conductivity of each component. κ' is the total thermal conductance of TET with 100 pairs of TE pillars.

(3) As seen in Fig. 3d, there is air trapped between top and bottom textile layers. Based on the actual size of this part, we estimated the area percentage is 90%, which is calculated based on the total textile layer that do not cover on p-type or n-type segments.

(4) The total thermal conductance of the TET consisting of 100 pairs of TE pillars can be estimated as followed:

$$\kappa_{p,1,2,3}^{'} = \left(\frac{L_p}{\kappa_p A_p} + \sum_i^{1,2,3} \frac{2L_i}{\kappa_i A_i} \right)^{-1}$$

$$\kappa_{n,1,2,3}^{'} = \left(\frac{L_n}{\kappa_n A_n} + \sum_i^{1,2,3} \frac{2L_i}{\kappa_i A_i} \right)^{-1}$$

$$\kappa_{4,5}^{'} = \left(\frac{2L_4}{\kappa_4 A_4} + \frac{L_5}{\kappa_5 A_5} \right)^{-1}, \quad \kappa_6^{'} = \frac{\kappa_6 A_6}{L_6}$$

$$\kappa_{total}^{'} = 100 \times \left(\kappa_{p,1,2,3}^{'} + \kappa_{n,1,2,3}^{'} + \kappa_{4,5}^{'} + \kappa_6^{'} \right)$$

$$thermal\ resistance = A / \kappa_{total}^{'}$$

To evaluate the reliability of the calculation of TET, we measured the thermal resistance and CLO of a fabric without TE pillars using a fabric thermal resistance measurement system (YG606E), it was measured to be $1/\kappa_{fabric}^{'}$~0.0878 m^2K/W and 0.5664 clo, respectively. By using the size of TET and the thermal conductance of TE pillars, the total thermal conductance of TET with size of 15 cm × 9 cm can also be estimated as $\kappa_{total}^{'} = \left(\frac{\kappa_{pA_p}}{L_p} + \frac{\kappa_n A_n}{L_n} \right) \times 100 + 15 \times 9 \times 10^{-4} \kappa_{fabric}^{'} = 0.522\ W/K$, which agrees well with the above calculated one. Thus, we can assure that the estimation of thermal resistance of TET is reliable.

Table S5 The calculation of cooling capacity of TET with 100 pairs of TE pillars

S_{TET} (V/K)	T_2 at hot side (K)	ΔT (K)	r (Ω)	κ' (W/K)	Size of TET (m^2)	Equation
0.042	300	1	4.4	0.5335	0.0135	$Q_c = S_{TET}(T_2 - \Delta T) - \frac{1}{2}I^2 r - \kappa' \cdot$ $COP = \frac{Q_c}{I^2 r + S_{TET}\Delta T}$
		3				
		5				
		8				
		10				
		11.8				

Table S6 The calculation parameters of maximum achievable ΔT of TET

S_{TET} (V/K)	r (Ω)	κ' (W/K)	T_2 (K)	$z = \frac{S_{TET}^2}{r\kappa'}$ (K^{-1})	$T_{1,min} = \frac{\sqrt{1 + 2zT_2} - 1}{Z}$ (K)	$\Delta T_{max} = T_2 - T_{1,min}$ (K)
0.042	4.4	0.5335	300	2.05×10^{-3}	272.2	27.8

Table S7 The summary of the cooling effect and specific cooling capacity of our TET system with other wearable cooling technologies reported in the literature.

Cooling technology	Materials	Cooling effect (K)	Time duration (min)	Cooling capacity (W/m^2)	reference
Phase change material	Na_2SO_4/H_2O/ additives + polyester vest	3	210	29.1	19
	Na_2SO_4/H_2O/ additives + cotton/polyester with 72 mesh liner	1.1±0.2	125	70	20
	Ice + cotton vest with plastic holders	10	>60	74	21
	Na_2SO_4/H_2O/ additives +polyester vest	14	>60	46.7	22
Radiative cooling*	ZnO nanoparticles/nanoporous PE nanofiber textile	>10	-	>200	23
	APS-modified $AlPO_4$ particles/CMC + cotton textile	4.4	-	-	24
	Micrometer-sized SiO_2 + TPX	-		>110	25
	PTFE layer + TiO_2 nanoparticles/ PLA microfibers textile	4.8	-	-	26
	nanoporous PE textile	2.7	-	-	27
	PEO micro/nanofibers film	5	-	110	28
Electrocaloric cooling	P(VDF-TrFE-CFE) film	3.6	-	2.8 W/g	29
Thermoelectric cooling	Ag_2Se, PEDOT:PSS+ silica elastomer	10	-	256	30
	commercial bismuth telluride	8.2	-	1300	31

* The cooling data of the majority of radiative cooling textiles were based on the comparison with untreated cotton fabrics.

References

1. M. B. Kleiner, S. Kuhn and K. Haberger, *IEEE Transactions on Components, Packaging, and Manufacturing Technology: Part A*, 1995, **18**, 795-804.
2. R. Chein and G. Huang, *Applied Thermal Engineering*, 2004, **24**, 2207-2217.
3. Y.-W. Chang, C.-C. Chang, M.-T. Ke and S.-L. Chen, *Applied Thermal Engineering*, 2009, **29**, 2731-2737.
4. Y. Shiming and T. Wenshuan, *Heat transfer*, China Higher Education Press, 2006.
5. A. F. Ioffe, L. S. Stil'bans, E. K. Iordanishvili, T. S. Stavitskaya, A. Gelbtuch and G. H. Vineyard, *Semiconductor thermoelements and thermoelectric cooling*, Physics Today, 1959, **12**, 42
6. C. Goupil, W. Seifert, K. Zabrocki, E. Müller and G. J. Snyder, *Entropy*, 2011, **13**, 1481-1517.
7. V. Leonov and R. Vullers, *Journal of electronic materials*, 2009, **38**, 1491-1498.
8. V. Leonov and R. Vullers, ECT07, 2007, **5**, 47-52
9. M. Zadan, M. H. Malakooti and C. Majidi, *ACS applied materials & interfaces*, 2020, **12**, 17921-17928.
10. Y. Yang, H. Hu, Z. Chen, Z. Wang, L. Jiang, G. Lu, X. Li, R. Chen, J. Jin and H. Kang, *Nano letters*, 2020, **20**, 4445-4453.
11. Y. Ekubaru, T. Sugahara, K. Ibano, A. Suetake, M. Tsurumoto, N. Kagami and K. Suganuma, *Advanced Materials Technologies*, 2020, **5**, 1901128.
12. F. Suarez, D. P. Parekh, C. Ladd, D. Vashaee, M. D. Dickey and M. C. Öztürk, *Applied energy*, 2017, **202**, 736-745.
13. S. J. Kim, H. E. Lee, H. Choi, Y. Kim, J. H. We, J. S. Shin, K. J. Lee and B. J. Cho, *ACS nano*, 2016, **10**, 10851-10857.
14. T. Varghese, C. Dun, N. Kempf, M. Saeidi-Javash, C. Karthik, J. Richardson, C. Hollar, D. Estrada and Y. Zhang, *Advanced Functional Materials*, 2020, **30**, 1905796.
15. W. Yang, X. Du, J. Zhao, Z. Chen, J. Li, J. Xie, Y. Zhang, Z. Cui, Q. Kong and Z. Zhao, *Joule*, 2020, **4**, 1557-1574.
16. C. Jiang, Y. Ding, K. Cai, L. Tong, Y. Lu, W. Zhao and P. Wei, *ACS applied materials & interfaces*, 2020, **12**, 9646-9655.
17. E. Kim, J. Lee, D. Kim, K. E. Lee, S. S. Han, N. Lim, J. Kang, C. G. Park and K. Kim, *Chemical communications*, 2009, **12**, 1472-1474.
18. T. Ding, K. H. Chan, Y. Zhou, X.-Q. Wang, Y. Cheng, T. Li and G. W. Ho, *Nature communications*, 2020, **11**, 6006.
19. C. Gao, K. Kuklane, F. Wang and I. Holmer, *Indoor Air*, 2012, **22**, 523-530.
20. Q. Ying Ke and H. Wang, *International Journal of Occupational Safety and Ergonomics*, 2020, **26**, 1-11.
21. J. Smolander, K. Kuklane, D. Gavhed, H. Nilsson and I. Holmér, *International journal of occupational safety and ergonomics*, 2004, **10**, 111-117.
22. C. Gao, K. Kuklane and I. Holmer, *Ergonomics*, 2010, **53**, 716-723.
23. L. Cai, A. Y. Song, W. Li, P. C. Hsu, D. Lin, P. B. Catrysse, Y. Liu, Y. Peng, J. Chen, H. Wang, J. Xu, A. Yang, S. Fan and Y. Cui, *Adv Mater*, 2018, **30**, e1802152.
24. S. Zhong, L. Yi, J. Zhang, T. Xu, L. Xu, X. Zhang, T. Zuo and Y. Cai, *Chemical Engineering Journal*, 2021, **407**.
25. Y. M. Yao Zhai, Sabrina N. David, Dongliang Zhao, Runnan Lou, Gang Tan, Ronggui Yang,

Xiaobo Yin, *Science*, 2017, **355,** 1062–1066.

26. S. P. Shaoning Zeng, Minyu Su, Zhuning Wang, Maoqi Wu, Xinhang Liu, Mingyue Chen, Yuanzhuo Xiang, Jiawei Wu, Manni Zhang, Qingqing Cen, Yuwei Tang, Xianheng Zhou, Zhiheng Huang, Rui Wang, Alitenai Tunuhe, Xiyu Sun, Zhigang Xia, Mingwei Tian, Min Chen, Xiao Ma, Lvyun Yang, Jun Zhou, Huamin Zhou, Qing Yang, Xin Li, Yaoguang Ma, Guangming Tao, *Science* 2021, **373,** 692–696.
27. A. Y. S. Po-Chun Hsu, Peter B. Catrysse, Chong Liu, Yucan Peng, Jin Xie, Shanhui Fan, Yi Cui, *Science*, 2016, **353,** 1019-1023.
28. D. Li, X. Liu, W. Li, Z. Lin, B. Zhu, Z. Li, J. Li, B. Li, S. Fan, J. Xie and J. Zhu, *Nat Nanotechnol*, 2021, **16**, 153-158.
29. Z. Z. Rujun Ma, Kwing Tong, David Huber, Roy Kornbluh, Yongho Sungtaek Ju, Qibing Pei, *Science*, 2017, **357,** 1130–1134.
30. S. Xu, M. Li, Y. Dai, M. Hong, Q. Sun, W. Lyu, T. Liu, Y. Wang, J. Zou, Z. G. Chen and M. Dargusch, *Adv. Mater.*, 2022, **34**, e2204508.
31. R. A. Kishore, A. Nozariasbmarz, B. Poudel, M. Sanghadasa and S. Priya, *Nature communications*, 2019, **10**, 1765.